Remote Detection of TPS Failure Using Millimeter-Wave Radiometry

Final Report

University of Michigan Technical Report 035983-F

NASA Grant: NCC 2-5224

Submitted to: Dr. Joan Salute
Thermoscience Institutue
NASA Ames Research Center
Mail Stop 234-1
Moffett Field, CA 94035
(650) 604-0332

Submitted by: Mr. M. Craig Dobson
Mr. Todd Clancy
Dr. Fawwaz T. Ulaby

Submission Date: July 1999

Table of Contents

1.0 Introduction

This technical report is the final report for NASA Grant NCC 2-5224 and document research performed to examine the feasibility of using microwave and millimeter wave techniques to examine failure modes in the Thermal Protection System (TPS) of the space shuttle. The Thermal Protection System (TPS) makes possible the safe re-entry of the Reusable Launch Vehicle (RLV) into the earth's atmosphere. Maintenance of the TPS is performed between every launch and consists of visually inspecting each of the 25,000 shuttle tiles for surface damage and thermal breaches. This takes many man-hours and is very costly. It is believed that millimeter-wave techniques combined with automated vehicle health monitoring may be used to reduce the considerable expense of this task. Extensive surface damage is readily detectable by optical techniques, so the application of passive remote sensing will be on the thermal breeches that occur under the tile surfaces.

This technical report describes the potential of millimeterwave radiometry for the detection of failure in the Shuttle's Thermal Protection System (TPS) and reports on the development of a the 94 GHz radiometer system to detect subsurface gaps in the TPS caused by charred strain isolation pad (SIP). With this system it is possible to:

a) Characterize the permittivity of the TPS materials including the Reusable Surface Insulation (RSI), the Strain Isolation Pad (SIP), and bonding materials,
b) Use the results of (a) to simulate TPS emission, and
c) Measure various tiles, both damaged and undamaged, to evaluate the proposed technique.

The reasons for measurement with millimeterwave remote sensing are twofold:

1. Spatial resolution (both depth and width) is generally limited to a fraction of a wavelength thus presenting millimeterwaves ($\lambda \leq 0.1$ cm)[1] as superior to microwaves.
2. The RSI is partially transparent at microwave and millimeter waves, but becomes opaque at higher frequencies (i.e. optical inspection is limited to the tiles surfaces). Thus air gaps and dielectric changes occurring underneath the tile may be remotely detected and imaged.

Preliminary experiments were done and computer models were created to test the hypothesis of TPS failure detection. The initial simulation results show that the natural emission of the TPS varies as a function of wavelength, incidence angle, and tile thickness. To simulate TPS failure due to charred SIP, air gaps were simulated underneath the RSI. Again, the emissivity of the TPS was shown to vary with air gap thickness. The variation was oscillatory as a function of all four sensing parameters. From these results, we conclude that a millimeterwave measurement technique sensitive to emissivity changes of less than 0.01 would be sufficient to remotely detect charred SIP that causes air gaps of 0.05 mm. To eliminate gap size ambiguity, a two-frequency technique may be employed or a one-frequency technique with two different incidence angles may be used.

In order to further this research, a 94 GHz passive radiometer was designed and constructed with an average sensitivity of 0.4 degree Kelvin[2]. Calibration procedures were developed and, to test the validity of the project, preliminary measurements were performed on damaged and undamaged TPS samples provided by NASA. The results showed that emissivity changed by 0.033 between the two tiles and that emissivity changes of greater than 0.0014 are detectable by the system.

NASA has posed the following questions in connection to passive remote sensing of TPS materials:

(1) Can one distinguish between the clutter or background radiation and the small changes in signal caused by changes in material properties?
(2) How does one distinguish between changes in emissivity and changes in local temperature?
(3) Can sufficient transverse spatial resolution be achieved to localize the damaged area?

---

[1] λ is the wavelength.

[2] Sensitivities are measured with a one-second integration time unless otherwise stated.

(4) How can one distinguish between different types of damage?
(5) How can one accelerate the measurement and hence reduce the time for inspection?

In brief we found that:
(1) To distinguish between background clutter and the small changes in tile emissivity a cold load is used as the background. This is done experimentally by reflecting sky brightness temperatures off of the tile surface and in practice a liquid nitrogen cooled absorber can be used.
(2) Measuring the local temperature of the TPS eliminates it as a variable. The measurement can be done on the exterior of the TPS, assuming the tile layers have reached equilibrium. Immediately following Shuttle's landing, temperature gradients within the TPS would make this difficult.
(3) How much resolution does the application require? If resolution is required to be the width of a given tile (≈ 6-in.) then a single antenna will be sufficient. By use of millimeter wavelengths resolution is improved over microwave techniques. Resolution may be further improved by use of arrays or synthetic aperture techniques.
(4) Two techniques may be used to investigate the radiometer's response to different types of damage: (a) simulations can be performed based on information from NASA/Ames detailing the types of failures that may be present, and (b) experiments can be done to characterize the response of the 94 GHz radiometer system to the various failure modes. More work must be done in this area before firm conclusions can be drawn.
(5) We can accelerate the measurement and hence reduce the time for inspection by using short integration times, scanning the antenna beam either electrically or mechanically, and by automating the process.

The remainder of the report is divided into 4 sections. First, in Section 2 we describe the dielectric properties of TPS materials, simulations of TPS emission and measurements. Then in Section 3 we give a system level description of the 94 GHz radiometer constructed to further the goals of this project. Section 4 provides details of system performance. Finally, discussion, conclusions and a plan for further research are given in Section 5.

2.0 Emission by the Thermal Protection System

The TPS consists of stacked tile structures typically of the following: A silica-based upper layer (RSI) with a TUFI coating bonded to a strain isolation pad (SIP, Nomex felt, or SIP) layer with Room Temperature Vulcanized Membrane (RTV). The whole assembly is then bonded to an aluminum backing with RTV (*Figure 2.1*).

Figure 2.1: Thermal Protection System (Stacked tile structure)

2.1 Dielectric Measurements

NASA/Ames Research Center provided a number of tile samples. The dielectric properties of the materials were measured at 15, 16 and 94 GHz. Materials used in the construction of the RSI include SIRCA, FRCI-12, SIRCA-12, AETB-8 (dark and lite), and PICA. SIRCA-12 was also measured at 1.24 GHz.

2.1.1 Low Frequency Measurements

The low frequency measurements were performed using the techniques presented by El-Rayes and Ulaby, "Microwave Dielectric Spectrum of Vegetation—Part I: Experimental Observations"[3]. Coaxial probes were used in conjunction with a reflectometer system to measure the amplitude and phase of the reflection coefficient of the probe terminated in the material under test. The input reflection coefficient at the probe end is,

$$\rho = \frac{Z_L - Z_0}{Z_L + Z_0} = \frac{Y_0 - Y_L}{Y_0 + Y_L} \tag{2.1}$$

where $Y = 1/Z$, Z_0 is the line impedance, and Z_L is the load impedance, which is governed by the dielectric constant of the material and the geometry of the probe tip. An open-ended coaxial line may be represented by the equivalent circuit shown in *Figure 2.2*. If we place the probe in contact with a dielectric slab of infinite electrical thickness the admittance of the line is given by,

$$Y_L(\omega,\varepsilon) = Y_i(\omega) + Y_e(\omega,\varepsilon) \tag{2.2}$$

where $Y_i(\omega) = j\omega C_i$ is the "internal" admittance caused by the fringing capacitance C_i which accounts for the field in the region between the inner and outer conductors of the coax. The "external" admittance Y_e, consists of a frequency-dependant capacitor $C(\omega,\varepsilon)$ in parallel with a radiation conductance $G(\omega,\varepsilon)$

$$Y_e(\omega,\varepsilon) = j\omega C(\omega,\varepsilon) + G(\omega,\varepsilon) \tag{2.3}$$

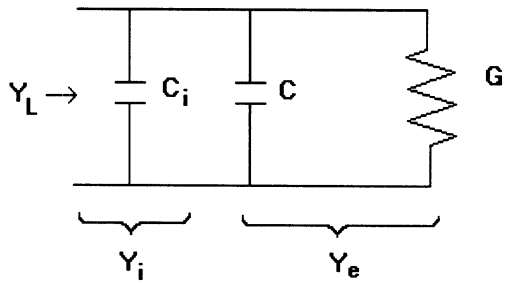

Figure 2.2: Probe equivalent circuit.

The capacitance C represents the fringing field concentration in the slab, and the conductance G represents the radiation into the medium. In free space C and G may be represented by,

$$\begin{aligned} C(\omega,\varepsilon_0) &= C_0 + B\omega^2 \\ G(\omega,\varepsilon_0) &= A\omega^4 \end{aligned} \tag{2.4}$$

To relate the admittance of the probe in free space to its admittance with the dielectric the following equation is used,

$$Y_e(\omega,\varepsilon) = \sqrt{\frac{\varepsilon}{\varepsilon_0}}\, Y_e\left(\omega\sqrt{\frac{\varepsilon}{\varepsilon_0}}, \varepsilon_0\right) \tag{2.5}$$

[3] TRGS Vol. 25, no. 5, 1987.

which allows us to write the total input admittance as,

$$Y_L(\omega,\varepsilon) = j\omega C_i + j\omega\varepsilon_r C_0 + j\omega^3\varepsilon_r^2 B + A\omega^4\varepsilon_r^{2.5} \qquad (2.6)$$

where $\varepsilon/\varepsilon_0$ has been replaced by ε_r. With the line admittance Y_0 known, measurements of ρ by a network analyzer lead directly to measurements of Y_L. To determine ε from Y_L we 1) calibrate the probe in order to determine the constants C_i, C_0, B, A, and 2) develop an iterative program for finding a value for ε that minimizes the error between the measured value of Y_L and the calculated value from *Equation 2.6*.

2.1.2 High Frequency Measurements

At 94 GHz a free space technique was employed to obtain the permittivity of the materials and is illustrated in *Figure 2.3*. Three measurements were performed. First a conducting plate was placed in front of the dielectric such that the reflectivity $\Gamma_1 = 1$. Then the plate was moved to the back of the material such that $\Gamma_2 = 1$. The final measurement was performed without the plate.

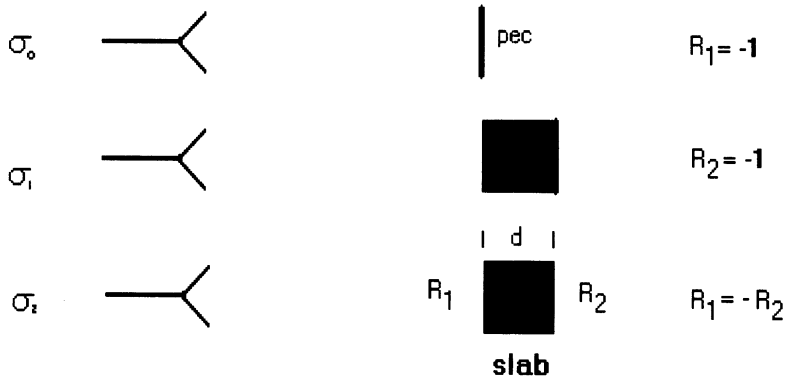

Figure 2.3: Free space permittivity measurements.

During the first measurement the antennas and target were oriented to obtain a maximum response and this was related to the *radar cross section* σ_0. For an equivalent infinite slab our free space radar measurements provide three radar cross sections and the following equations,

$$\Gamma_{C1} = \frac{\sigma_1}{\sigma_0}$$
$$\Gamma_{C2} = \frac{\sigma_2}{\sigma_0} \qquad (2.7)$$

where,

$$\Gamma_C = \frac{\Gamma_1 + \frac{\Gamma_2}{L_2^2} + 2\frac{\sqrt{\Gamma_1\Gamma_2}}{L_2}\cos(2\beta_2 d + \phi_1 - \phi_2)}{1 + \frac{\Gamma_1\Gamma_2}{L_2^2} + 2\frac{\sqrt{\Gamma_1\Gamma_2}}{L_2}\cos(2\beta_2 d + \phi_1 - \phi_2)} \qquad (2.8)^4$$

and,
$\Gamma_1 = |R_1|^2$
$\Gamma_2 = |R_2|^2$
$R_1 = |R_1|\angle\phi_1$

[4] Ulaby *et al.*, Microwave Remote Sensing, vol. 1 pp. 233-237, 1981.

$R_2 = |R_2| \angle \phi_2$
L_2 is the loss factor and is equal to $exp(2\alpha_2 d/cos\theta_2)$.
d is the thickness of the slab.
α_2 is the attenuation coefficient of the slab.
β_2 is the propagation coefficient of the slab and id equal to $2\pi n/\lambda$.
θ_2 is the incidence angle which we set to zero.
$n = sqrt(\varepsilon')$ is the index of refraction.

However d cannot be measured accurately enough to ensure a unique solution. For the silica-based materials, α_2 is high enough to warrant the following approximation.

$$\cos(2\beta_2 d + \phi_1 + \phi_2) = 0 \tag{2.9}$$

This simplifies *2.8* greatly and by putting *Equation 2.7* into *2.9* they yield two equations and two unknowns (n and α_2). The real permittivity is readily obtained by taking the square root of n, and the imaginary part is found by inverting,

$$\alpha_2 = \frac{2\pi}{\lambda}\left\{\frac{\varepsilon_r'}{2}\left[\left(1+\frac{\varepsilon_r''}{\varepsilon_r'}\right)^{1/2} - 1\right]\right\}^{1/2} \tag{2.9a}$$

The table below lists the dielectric properties of these materials. Their properties are very similar except for the pica, which is highly conductive and therefore impenetrable by millimeterwaves.

MATERIAL	Freq. (GHz)	ε'	ε"	α (dB/cm)
SIRCA	15	1.455	-0.127	
	16	1.502	-0.141	
	94	1.298	-0.00806	0.345
FRCI-12	15	1.325	-0.102	
	16	1.405	-0.115	
	94	1.253	-0.00620	0.265
SIRCA-12	1.24	1.350	-0.0188	
	15	1.535	-0.145	
	16	1.598	-0.159	
	94	1.159	-0.0273	1.169
AETB-8 (Dark)	15	2.313	-0.327	
	16	2.373	-0.367	
AETB-8[5]	94	2.280	-0.00784	0.335
AETB-8 (Lite)	15	1.209	-0.067	
	16	1.239	-0.072	
PICA	15	20.41	-25.1	
	94	195	-0.00706	0.302

These measurements verify that the silica-based tile material are transparent at microwave and millimeter-wavelengths and that that the RSI has an ε' of approximately 1.3 and an attenuation factor of 0.3 dB/cm, thus yielding excellent penetration. The TUFI coating on the AETB-8 has an ε' of approximately 2.3. The TUFI layer is however very thin and its effects on emissivity were not incorporated into this model. The effect of the RTV on emissivity was also ignored for the same reason. We are thus modeling a three-layered dielectric structure consisting of the following:

[5] Both dark and lite aetb-8.

1. Silicon ($\varepsilon_r \approx 1.3$, $\alpha \approx 0.3$ dB/cm , 2" thick)
2. Nomex felt ($\varepsilon_r \approx 1.3$, $\alpha \approx 0.3$ dB/cm, 1 cm thick)[6]
3. Aluminum ($\Gamma = -1$)

Where ε_r is the relative permittivity, α is the loss factor, and Γ is the reflection coefficient.

2.2 Emissivity of a Multi-layered Dielectric Structure

To determine the sensitivity of material emissivity to small air gaps formed between charred SIP and the silica two independent approaches were undertaken. Both methods solve for the emissivity of the layered structure and produce very similar results, hence confirming their validity. In this section we will examine one of the methods applied to the *n*-layered medium shown in *Figure 2.4*[7].

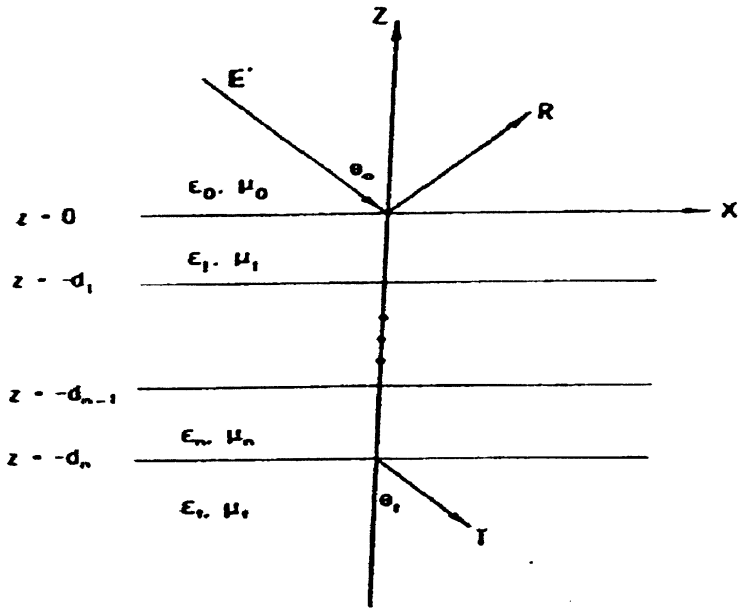

Figure 2.4: Reflection and transmission for an n-layer medium.

We assume a horizontally polarized incident electric field intensity,

$$E^i = \hat{y}E_y = \hat{y}\exp(jwt - jk_0 x\sin\theta_0 + jk_0 z\cos\theta_0) \tag{2.10}$$

and apply the Helmholtz wave equation at an arbitrary specular surface given here,

$$\left(\nabla^2 - k^2\right)\bar{E}(\bar{r}) = 0 \tag{2.11}$$

In any layer, the following form governs the electric field intensity,

$$\left(\frac{\partial^2}{\partial x^2} + \frac{\partial^2}{\partial z^2} + k_m^2\right)E_y = 0 \tag{2.12}$$

Assuming an e^{jwt} dependence, the solution to *2.12* for the *m*th layer is then,

[6] The actual permittivity of the Nomex felt was not measured in the preliminary experiment. This is one of the objectives of the new 94 GHz radiometer.

[7] Ulaby *et al.*, Microwave Remote Sensing, vol. 1 pp. 78 – 82, 1981.

$$E_{ym} = \left(A_m e^{jk_{zm}z} + C_m e^{-jk_{zm}z}\right) e^{-jk_0 x \sin\theta_0} \tag{2.13}$$

From Maxwell's equations, the corresponding magnetic field intensities are,

$$\begin{aligned} H_{xm} &= \frac{k_{zm}}{\omega\mu_m}\left(A_m e^{jk_{zm}z} - C_m e^{-jk_{zm}z}\right) e^{-jk_0 x \sin\theta_0} \\ H_{zm} &= \frac{k_0 \sin\theta_0}{\omega\mu_m}\left(A_m e^{jk_{zm}z} + C_m e^{-jk_{zm}z}\right) e^{-jk_0 x \sin\theta_0} \end{aligned} \tag{2.14}$$

k_{zm} is found by substituting *2.13* into *2.12*, and is given by,

$$k_{zm} = \sqrt{\omega^2 \mu_m \varepsilon_m - k_0^2 \sin^2\theta_0} \tag{2.15}$$

The boundary conditions are applied to relate the amplitudes A_m, C_m to the amplitudes A_{m+1},C_{m+1} of the successive dielectric interfaces. From the continuity of tangential electric fields,

$$A_m e^{jk_{zm}d_m} + C_m e^{-jk_{zm}d_m} = A_{m+1} e^{jk_{z(m+1)}v} + C_{m+1} e^{-jk_{z(m+1)}d_m} \tag{2.16}$$

And from the continuity of tangential magnetic fields,

$$\begin{aligned} \mu_{m+1} k_{zm} &\left(A_m e^{jk_{zm}d_m} - C_m e^{-jk_{zm}d_m}\right) \\ &= \mu_m k_{z(m+1)} \left(A_{m+1} e^{jk_{z(m+1)}d_m} - C_{m+1} e^{-jk_{z(m+1)}d_m}\right) \end{aligned} \tag{2.17}$$

Equations 2.16 and *2.17* may be combined in matrix form as

$$\begin{bmatrix} A_m e^{-jk_{zm}d_m} \\ C_m e^{jk_{zm}d_m} \end{bmatrix} = B_{m(m+1)} \begin{bmatrix} A_{m+1} e^{-jk_{z(m+1)}d_m} \\ C_{m+1} e^{jk_{z(m+1)}d_m} \end{bmatrix} \tag{2.18}$$

where,

$$B_{m(m+1)} = \frac{1}{2} \begin{bmatrix} 1 + \dfrac{\mu_m k_{z(m+1)}}{\mu_{m+1} k_{zm}} & \\ & \end{bmatrix} \leftrightarrow \begin{bmatrix} e^{jk_{z(m+1)}(d_{m+1}-d_m)} & R_{m(m+1)} e^{-jk_{z(m+1)}(d_{m+1}-d_m)} \\ R_{m(m+1)} e^{jk_{z(m+1)}(d_{m+1}-d_m)} & e^{-jk_{z(m+1)}(d_{m+1}-d_m)} \end{bmatrix} \tag{2.19}$$

and,

$$R_{m(m+1)} = \frac{\mu_{m+1} k_{zm} - \mu_m k_{z(m+1)}}{\mu_{m+1} k_{zm} + \mu_m k_{z(m+1)}} \tag{2.20}$$

where R is the Fresnel reflection coefficient for a horizontally polarized wave at the *boundary z* =

$-d_m$. The matrix $B_{m(m+1)}$ is referred to as the *backward propagation matrix*, because it permits A_m and C_m to be expressed in terms of $A_{m(m+1)}$ and $C_{m(m+1)}$. Correspondingly it is possible to express $A_{m(m+1)}$ and $C_{m(m+1)}$ in terms of A_m and C_m, and this would lead to a *forward propagation matrix* which is related to B by,

$$B_{m(m+1)}F_{m(m+1)} = I \tag{2.21}$$

We use the backward propagation matrix to compute the total reflection and total transmission coefficients R and T. The amplitudes of the total incident and total reflected electric fields may be related to the amplitudes in layer 1 by B_{01} and to those in layer 2 by $B_{01}B_{12}$ etc. For the semi-infinite medium below layer n there is only a transmitted field amplitude. The value of d_t in *2.18* can be an arbitrary finite number when we reach the boundary $z = -d_n$, since the d_t in the transmitted field will cancel with that in B_{nt}. Thus, the transmitted field is related to the incident and reflected fields by,

$$\begin{bmatrix} 1 \\ R \end{bmatrix} = B_{01}B_{12}\cdots B_{nt}\begin{bmatrix} Te^{jk_{zt}d_t} \\ 0 \end{bmatrix} \tag{2.22}$$

R and T can now be found using the two equations present in *2.22*. Emissivity is then given by

$$e(\theta) = 1 - \left|R(\theta)^2\right| \tag{2.23}$$

The above derivation was solved for horizontal polarization. To obtain the solution for vertical polarization duality is employed, i.e., replace **E**, **H**, ε, μ, by **H**, -**E**, μ, ε respectively. For the simple case of four dielectric layers and three interfaces (air – RSI – SIP – aluminum) where the transmission is zero the expression for the reflection coefficient for horizontal polarization is as follows,

$$R = \frac{\begin{array}{l}\left[\left(R_{01}+R_{12}e^{-j2k_{z1}d_1}\right)+\left(R_{01}R_{12}+e^{-j2k_{z1}d_1}\right)R_{23}e^{-j2k_{z2}d_2}\right] \\ -\left[\left(R_{01}+R_{12}e^{-j2k_{z1}d_1}\right)R_{23}+\left(R_{01}R_{12}+e^{-j2k_{z1}d_1}\right)e^{-j2k_{z2}d_2}\right]e^{-j2k_{z3}d_3}\end{array}}{\begin{array}{l}\left[\left(1+R_{01}R_{12}e^{-j2k_{z1}d_1}\right)+\left(R_{12}+R_{01}e^{-j2k_{z1}d_1}\right)R_{23}e^{-j2k_{z2}d_2}\right] \\ -\left[\left(1+R_{01}R_{12}e^{-j2k_{z1}d_1}\right)R_{23}+\left(R_{12}+R_{01}e^{-j2k_{z1}d_1}\right)e^{-j2k_{z2}d_2}\right]e^{-j2k_{z3}d_3}\end{array}} \tag{2.24}$$

where,

$$R_{01} = \frac{\mu_1 k_{z0} - \mu_0 k_{z1}}{\mu_1 k_{z0} + \mu_0 k_{z1}} \quad , \quad R_{12} = \frac{\mu_2 k_{z1} - \mu_1 k_{z2}}{\mu_2 k_{z1} + \mu_1 k_{z2}} \quad , \quad R_{23} = \frac{\mu_3 k_{z2} - \mu_2 k_{z3}}{\mu_3 k_{z2} + \mu_2 k_{z3}}$$

and,

$$k_{z0} = \sqrt{\omega^2 \mu_0 \varepsilon_0 - k_0^2 \sin^2 \theta_0} = k_0 \cos\theta_0$$

$$k_{z1} = \sqrt{\omega^2 \mu_1 \varepsilon_1 - k_0^2 \sin^2 \theta_0} = k_1 \cos\theta_1$$

$$k_{z2} = \sqrt{\omega^2 \mu_2 \varepsilon_2 - k_0^2 \sin^2 \theta_0} = k_2 \cos\theta_2$$

$$k_{z3} = \sqrt{\omega^2 \mu_3 \varepsilon_3 - k_0^2 \sin^2 \theta_0} = k_3 \cos\theta_2$$

2.3 Sample Calculations

The equations were solved and plotted in *Figures 2.5, 2.6,* and *2.7* as a function of incidence angle, tile thickness and frequency. In *Figure 2.5* the incidence angle was 20° and the tile thickness was 2". In *Figure 2.6* the frequency was set to 95 GHz and the tile thickness was 2". In *Figure 2.7* the incidence angle was 20° and the frequency was set to 95 GHz.

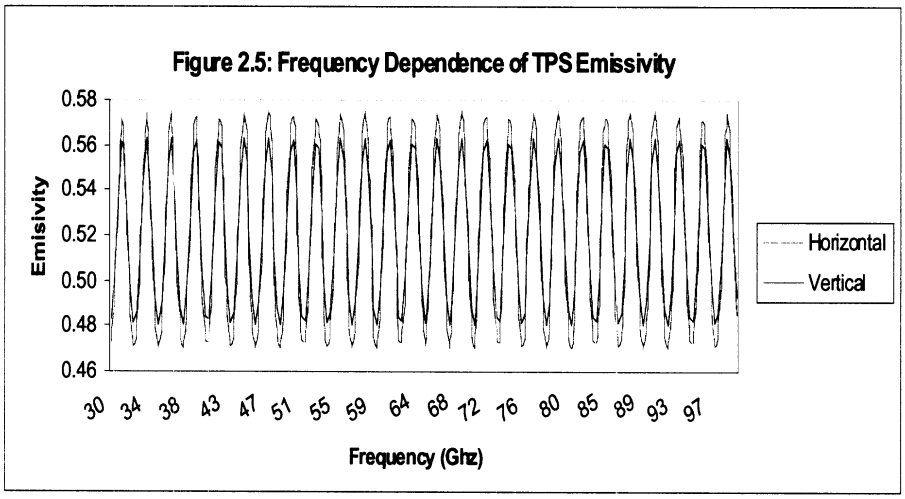

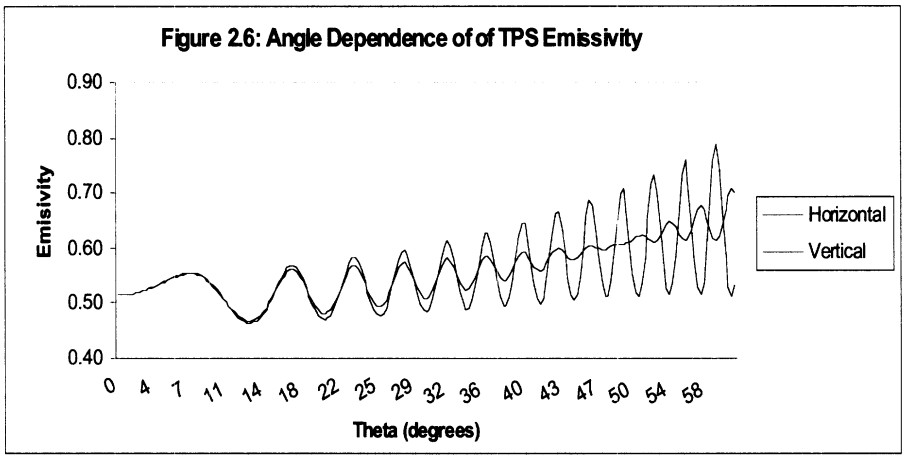

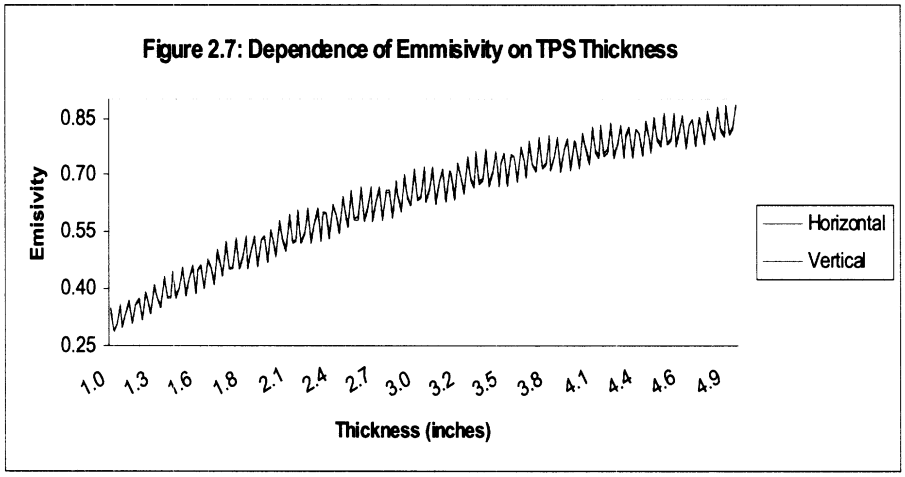

The emissivity of the TPS was calculated as a function of air gap thickness underneath a 2" tile and is shown in *Figure 2.8*. In this simulation an air gap was placed between the RSI and the SIP and was varied in size from 2 to 5 mm. The width of the RSI and SIP were held constant. This may occur if the tiles were somehow lifted from the surface of the shuttle. The oscillations shown in *Figure 2.8* are a result of resonance effects that vary as the total depth of the RSI-gap-SIP structure increases.

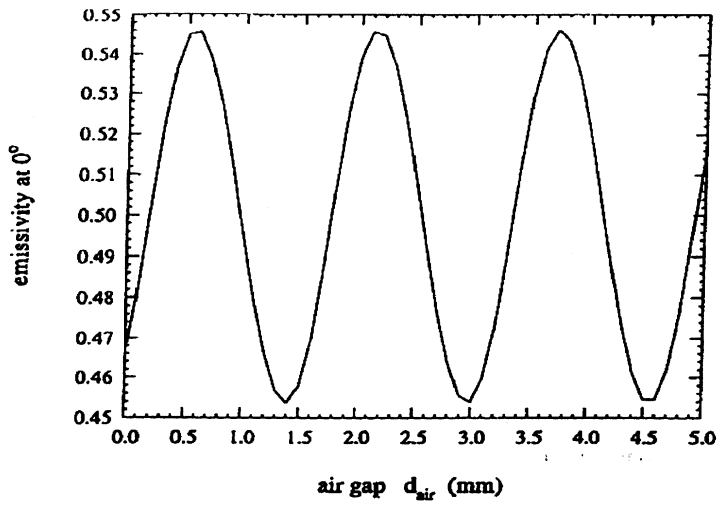

Figure 2.8: Variation of emissivity due to size of air gap.

Horizontally polarized radiation was found to have the greatest sensitivity to gap thickness, which is expected to be a maximum of 1.15 K/0.001" with a peak brightness temperature change of 38 K. For vertical polarization a maximum temperature change of 16 K is expected. In emissivity, we expect a change of 0.2/0.1 mm for horizontal polarization. Sensitivity to air gap thickness is seen to increase at incidence angles > 20°.

Another mode of TPS failure includes charred SIP, which also presents an air gap underneath the RSI.[8] This may be modeled by increasing the gap width while maintaining the total depth of the structure. As gap width increases, SIP width decreases. This is a better representation of the samples that NASA/Ames provided. *Figure 2.9* shows how emissivity changes with air gap size.

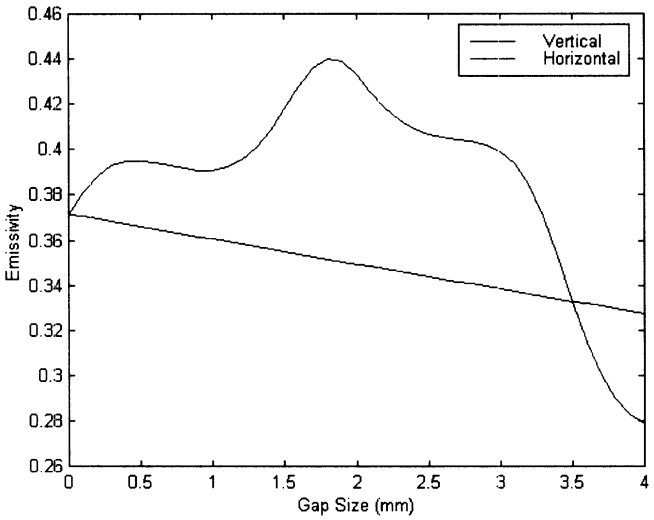

Figure 2.9: Variation of emissivity due to air gap size.

This simulation was done after the experiments of *Section 4.5* where the emissivity of an undamaged and a damaged tile were measured. The simulation was designed to replicate the same results and used the exact dimensions of the tiles measured. We compare the measured values with the model in *Section 4.5*.

RSI width	0.9"
SIP width (initial)	0.17"
SIP width (final)	0.0125"

The following conclusions can be drawn for these simulations:

1. The RSI is penetrable by millimeterwave radiation. The RSI is low loss and the SIP is practically lossless, yielding the ability to probe and possibly image the internal structure of the TPS.
2. Emissivity oscillates with frequency, incidence angle, tile thickness, and air gap size. This suggests that the use of one frequency at one incidence angle will be insufficient to determine whether emissivity changes are due to changes in tile thickness or air gaps below the surface. This suggests the use of (a) a two-frequency approach, or (b) a multi-angle approach, or (3) a change detection approach to resolve ambiguities.
3. The RSI is lossy enough to provide detectable changes in emissivity as a function of frequency, incidence angle, tile thickness, and air gap size. The application of passive remote sensing is facilitated by the conclusion that the tiles have some loss. For, although we want the tiles to be penetrable, if they where completely lossless, the aluminum back plate would

[8] This approach is equally applicable to detection of air gaps within the RSI.

reflect all energy yielding an effective emissivity of 1 regardless of frequency, incidence angle, tile thickness, and air gap size.

3.0 94 GHz Radiometer System

Due to the fact that we are trying to detect very small air gaps underneath a layered dielectric structure, millimeter-wave frequencies are employed to take advantage of their short wavelengths. A high frequency passive radiometer was designed for laboratory measurements. A 94 GHz Dicke type radiometer was chosen because of the availability of major component parts and the additional stability inherent in Dicke radiometers.

The radiometer system consists of three subsections listed below and pictured in *Figure 3.1*:

1. Radiometer – Including all front-end microwave and base-band components down to the crystal detector, mounted on an aluminum frame enclosed in an insulated aluminum box.
2. Power Supply Module – Houses various power supplies and the temperature controller.
3. Lock-In Amplifier – Stanford Research Systems SR850 DSP.

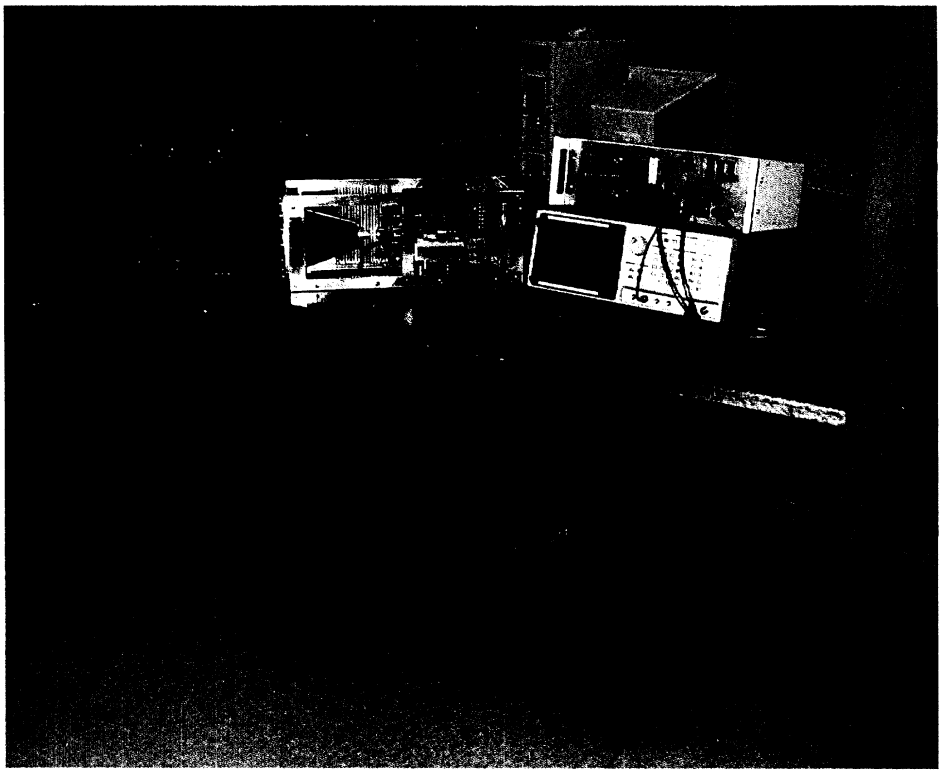

Figure 3.1: Radiometer System.

3.1 94 GHz Radiometer

The radiometer consists of a polystyrene insulated aluminum case and an aluminum frame that houses the front end and base-band signal processing components. Below is a list of the major components of the radiometer and *Figure 3.2* shows a block diagram of the system.

- Lens corrected conical horn antenna
- Ferrite switch (Dicke switch)
- Balanced mixer

- Amplifier (pre- and post IF)
- Detector

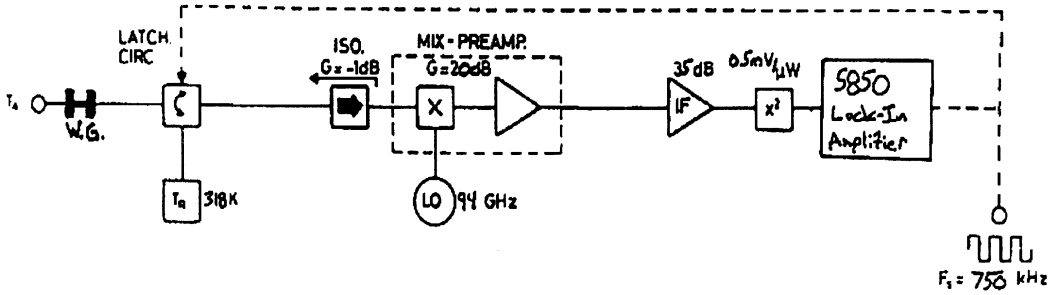

Figure 3.2: 94 GHz Radiometer

The signal flow throughout this Dicke radiometer proceeds as follows: The apparent temperature (T_A), based on the physical temperature and emissivity of the scene as viewed by the main beam of the antenna, passes through the antenna via a section of waveguide into the ferrite switch. The output of the switch is band limited to 2 GHz around 94 GHz. The antenna, waveguide, and switch are assumed to have bandwidths of approximately 2%. The switch is a three-port circulator that electrically directs two inputs to a single output at a switching rate of 750 kHz. The switching rate is controlled by a current driver, which is fed by a lock-in amplifier and is adjustable. The second input is connected to a reference dummy load that is temperature regulated to 45° C (T_R). In fact, all of the front-end components are located in an insulated box and maintained at this temperature. The termination has an effective emissivity of 1; thus its brightness temperature is equal to its physical temperature. The output of the Dicke is then a 750 kHz square wave modulated noise signal consisting of a high reference noise level and a low antenna temperature level.[9] This then passes through an isolator to a balanced double side band (DSB) mixer. The superheterodyne receiver makes use of the lower DSB noise figure of the balanced mixer to lower the system noise temperature (T_N) and improve sensitivity. The signal is mixed down to base-band and then enlarged by two amplifiers with gains of 20 and 35 dB respectively. The first amplifier limits the system bandwidth to from 10 MHz to 510 MHz. Thus the output of the amplifier is a 750 kHz modulated square wave with noise frequency components up to 510 MHz. Due to the use of DSB mixing, and a local oscillator center frequency of 94.2 GHz, all of the information from 93.69 GHz to 94.71 GHz is now present in the base-band signal. A square-law detector then removes the base-band modulation and outputs the square-wave riding on a bias level that is proportional to the noise temperature of the radiometer front end. The output peak-to-peak voltage of the detector is now proportional to the input apparent temperature and the total gain of the radiometer up to this point is 78 dB.[10].

The choice of a switching frequency (F_S) is governed by a few considerations. First, gain fluctuations cause instability in total power radiometers but have less effect in Dicke radiometers because the output represents only the difference between the antenna apparent temperature and the stable dummy load. This is true so long as the switching frequency is faster than any such fluctuations, which typically sets a lower limit of approximately 100 Hz. Second, it is clear that the integration time of the radiometer has to be much greater than $1/F_S$ to ensure the same number of cycles of antenna and reference temperatures are integrated. Given an expected integration time of 1 second, this sets a lower bound of, again, 100 Hz. Finally, the 5-μsec switching speed of the circulator dictates an upper bound to F_S. This switching time yields an uncertainty in the duty cycle of the Dicke. A 50% is a preconditional for all calculations concerning Dicke radiometers, thus leading to a maximum of:

[9] Any scene viewed by the antenna is expected to have an apparent temperature lower than 45° C

[10] This includes losses from the waveguide, ferrite switch, isolator, and insertion loss of the balanced mixer.

$$F_S < \frac{5}{t_s} \cdot 10^{-3}\ hz = 1000\ hz \tag{3.5}$$

where t_s is the integration time constant. Dicke radiometers are also very sensitive to noise near the switching frequency and to AC power line frequencies and their harmonics. A reasonable choice is then 750 MHz.

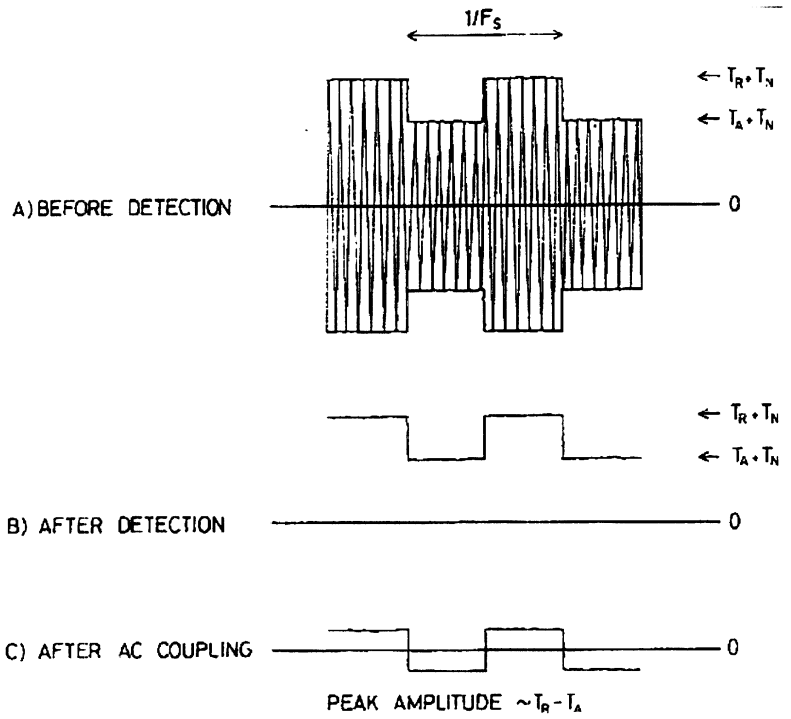

Figure 3.3: Signal pre- and post-detection.

Figure 3.3a and *3.3b* displays the signal form before and after detection. It is then passed through a coax cable into the lock-in amplifier were it is AC coupled and the RMS voltage is measured (*Figure 3.3c*). *Figure 3.4* shows the output of the radiometer as measured by an oscilloscope.[11]

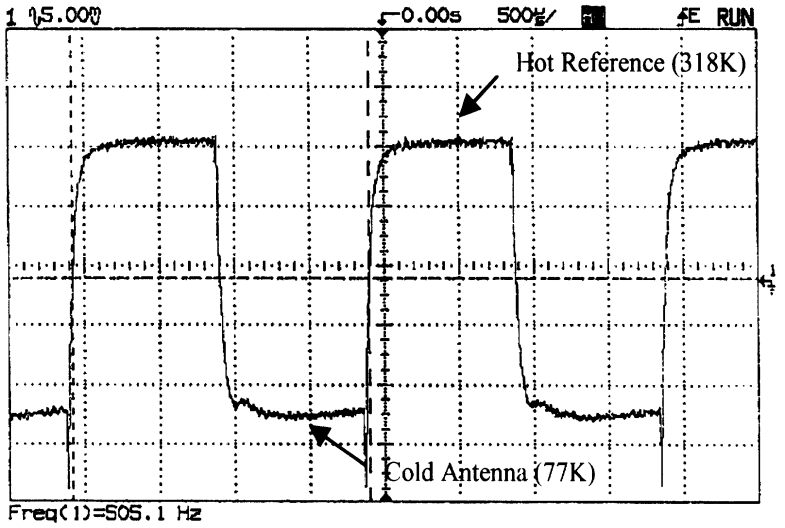

Figure 3.4: Radiometer output.

[11] This measurement was done in the early stages of the radiometer development and thus reflects a different switching rate (505 kHz).

Radiometers are particularly sensitive to temperature gradients, thus necessitating the use of temperature control. Heating to 45° C is accomplished by running current through a 3"x 6" resistive heating element mounted on a large heat sink. Air is then circulated throughout the insulated case by an AC fan[12] and the temperature is monitored with a sensor mounted on the dummy load of the Dicke switch. Temperature control is maintained to better than 0.1° C. *Figure 3.5* shows a picture of the front end of the radiometer including the base-band components and the two heat sinks. *Figure 3.6* is a picture of the radiometer out of its insulating case.

Figure 3.5: Radiometer front end.

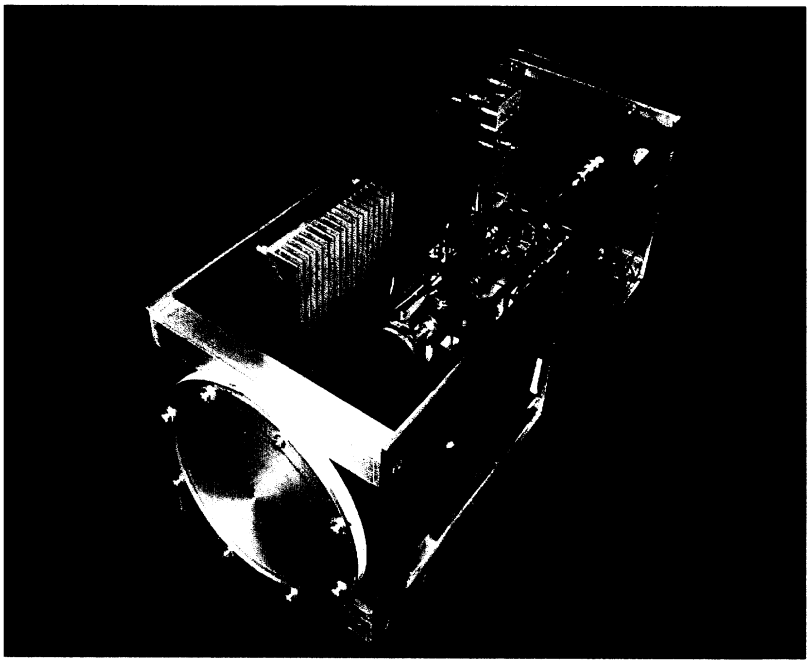

Figure 3.6: 94 GHz Radiometer.

[12] All Pictures show the DC fan which has sense been replaced by an AC fan.

3.2 Lock-In Amplifier

The lock-in provides the following:

- Amplification
- Stable switching frequency
- Precise signal detection
- Integration
- Data display and recording
- Statistical operations

The lock-in amplifier outputs the reference switching frequency to the power supply module and receives the square-wave output from the crystal detector in the radiometer. The square-wave input signal is digitally sampled and ac-coupled. It is then mixed with the input reference frequency and filtered, producing a DC voltage level proportional to the amplitude of the difference between the dummy load temperature and the apparent antenna temperature. Thus, a high output voltage indicates a low apparent temperature and a low output voltage indicates and apparent temperature close to 45° C, the physical temperature of the dummy load. The filtering process (integration) is what controls the relative sensitivity of the radiometer and is adjusted by time constants up to 30 seconds. Sensitivity is also effected by the effective roll-off of the filter, which can be set to 6, 12, 18 and 24 dB/oct. All measurements have been performed with the maximum filter roll-off of 24 dB/oct. The lock-in provides amplification both before and after the mixing to produce a signal level that is readable on its CRT display. Voltage readings on the display reflect the actual voltage level, before amplification, that is input to the lock-in. The data can be displayed as a function of time and recorded on a 3.5 floppy disk for transfer to a computer. One very convenient option on the lock-in is its ability to do statistical operations such as, calculate the mean and standard deviation (Vrms) of the voltage output over time.[13] This cuts down tremendously on the amount of data recording.

3.3 Power Supply Module

The power supply module is an aluminum and steel box that contains two Acopian power supplies, a relay, and a PID (proportional, integral, and differential) temperature controller. It was decided to have these components separate from the radiometer to limit EMI (electromagnetic interference) and to minimize its size and weight. The power supply module is connected to the radiometer via three cables. One 9-pin cable connection contains the 115-volt, 60 Hz, AC voltage supplying the heating element and fan, and 4 wires connecting the temperature controller to an RTD temperature sensor affixed to the dummy load of the Dicke switch. Another 9-pin cable passes the power supplying the LO, amplifiers, and current driver. It also passed the switching reference frequency from the lock-in to the current driver.

3.5 94 GHz Radiometer Specifications

Dimensions:	30x30x64 cm
Radiometer Type:	Dicke Switch
Receiver Type:	DSB balanced
Center Frequency:	94.2 GHz
Band-width:	500 MHz
Antenna Type:	Lens-corrected horn
Antenna Diameter:	15 cm
Antenna Beam-width:	1.5° (6 dB ~ 3°)
Switching Rate:	750 Hz
Footprint @ 2m:	5 cm (6 dB ~ 10 cm)
Radiometric Resolution:	< 1 K @ 1 sec
Calibration References:	(1) Room temp absorber

[13] Vrms is a direct measurement of the radiometer sensitivity.

	(2) Liquid N_2 absorber (3) Sky brightness (4) H_2O emissivity

4.0 System Tests and Calibration

This section contains the results of system tests and outlines the calibration procedures used with the 94 GHz radiometer. Radiometer calibration, sensitivity, and the stability of the system will be presented. Next we review measurement configurations and give results of test measurements performed on sample tiles.

4.1 Calibration

The governing equations that relate the output of the radiometer to the temperature of the scene as viewed by the antenna are given here:

$$T_{App} = a + bV_{out} \tag{4.1}$$

$$T_{App} = T_{Phy}e(\theta) + T_{inc}[1 - e(\theta)] \tag{4.2}$$

where,

T_{App} = apparent temperature viewed by the antenna.
V_{out} = output voltage of the radiometer,
T_{Phy} = the physical temperature of the target.
T_{inc} = incident radiation from the sky or other source.
e = the emissivity of the target.

Equation 4.1 simply expresses the assumption that the voltage output of the radiometer is linearly related to the apparent temperature of the scene as viewed by the antenna. This is the *transfer function* of the system. *Equation 4.2* states that the apparent temperature of an object viewed by the radiometer is equal to its effective brightness temperature, plus whatever incident radiation that is reflected off of its surface into the antenna. This assumes that there are negligible side lobes with a main beam efficiency of 100%. An object's effective brightness temperature (T_B) is the product of its physical temperature and its emissivity. In the standard setup we use for tile measurements (see *Figure 4.6A*) T_{inc} is equal to the sky brightness temperature T_{Sky}, and when viewing the sky alone (i.e. no tile target) T_{App} is just equal to T_{Sky}.

The purpose of calibration is to determine the constants a and b in *Equation 4.1*, thus establishing the relationship between the output voltage and the input antenna apparent temperature. If the relationship between emissivity and output voltage is desired, *Equation 4.2* can be used in conjunction with *4.1* to obtain a different system transfer function. The new transfer function is shown in *Equation 4.3* and requires that T_{Phy} and T_{inc} be known. In order to maximize the response of the system to changes in TPS emissivity, T_{inc} is kept as low as possible. This is done experimentally by using sky brightness temperatures, but any cold load will due.

$$e = \left(\frac{a - T_{inc}}{T_{Phy} - T_{inc}}\right) + \left(\frac{b}{T_{Phy} - T_{inc}}\right)V_{out} = a' + b'V_{out} \tag{4.3}$$

These are linear relations and would therefore require only two points to determine the characteristic transfer function. However, to ensure accuracy, we are attempting to employ more calibration points. The radiometer is calibrated using a variety of targets including distilled water, alcohols, room temperature absorber ("hot load"), liquid nitrogen (N2) saturated absorber ("cold load"), and sky brightness temperatures. Investigations into dry dielectrics such as sand, nylon, and tungsten bronze ferroelectrics are also being done.

4.1.1 Hot and Cold Loads

Hot and cold loads are by far the most common targets used in calibration and measurements are performed by placing an absorber (room temperature or N2 saturated) in the main beam of the antenna. Due to practical matters, the N2 saturated absorber used in the beginning of project was small in size and held directly against the antenna. It was hypothesized that this may effect the pattern of the antenna and cause a mismatch between the antenna and the rest of the radiometer system. This was tested in the laboratory by recording the voltage output while looking at room temperature absorber placed at varying distances from the antenna. *Figure 4.1* shows two traces; the first was conducted in the laboratory and the second was performed on the roof of the EECS building.

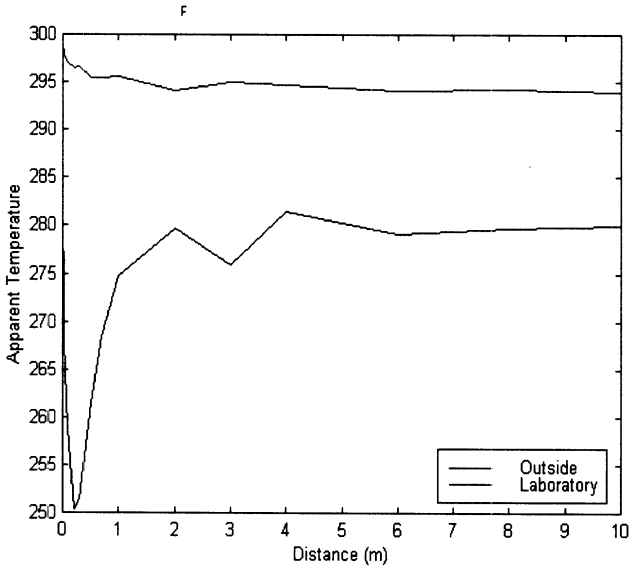

Figure 4.1: Absorber apparent temperature

The laboratory test results show that an absorber placed directly in front of the antenna had a temperature difference of 6 K from one to four meters away. The apparent temperature of the absorber changes abruptly and then levels off beyond 3 meters. In the laboratory, beyond 3 meters the temperature measurements had a standard deviation of approximately 0.4 Kelvin, which is the average system sensitivity, as described in *Section 4.2*. Outdoor tests on the roof of the EECS building revealed a much more dramatic effect than in the lab with variations of up to 40 Kelvin at close ranges. The output did again stabilize beyond 5 meters. For absolute accuracy in apparent temperature it was deemed necessary to place both hot and cold loads beyond this minimum distance. We do not however believe that this phenomenon will effect the sensitivity of the radiometer to detect relative changes in apparent temperature.

It was easy to place the hot load in the far field; but for the cold load, a foam bath was constructed to hold a 2.5 x 2.5 ft. piece of absorber saturated with liquid nitrogen. A metal plate was then used to direct the beam of the antenna down onto the absorber. The absorber is however corrugated (has peaks and valleys like an egg carton), causing the liquid nitrogen to drain out of the peaks of the absorber while it lay flat in the bath. The cold load voltage is obtained by letting the N2 boil off from above the peaks to below. The highest output voltage recorded is then used as the reference point.[14] Currently measurements are being performed to determine how much overall change occurs in the output voltage and if this change is consistent from measurement to measurement. If successful, we will no longer have to wait through the long boil-off period required above. A typical radiometer output is shown in *Figure 4.2*. As the nitrogen boils off over time, the electrical depth of the impedance mismatch at the N2 absorber boundary changes.

[14] The reference point is not assumed to be the boiling temperature of N2.

Thus we have the interference effect shown in the first 20 minutes of the measurement. After about 30 minutes there is no boundary to speak of and we can take our minimum reading.

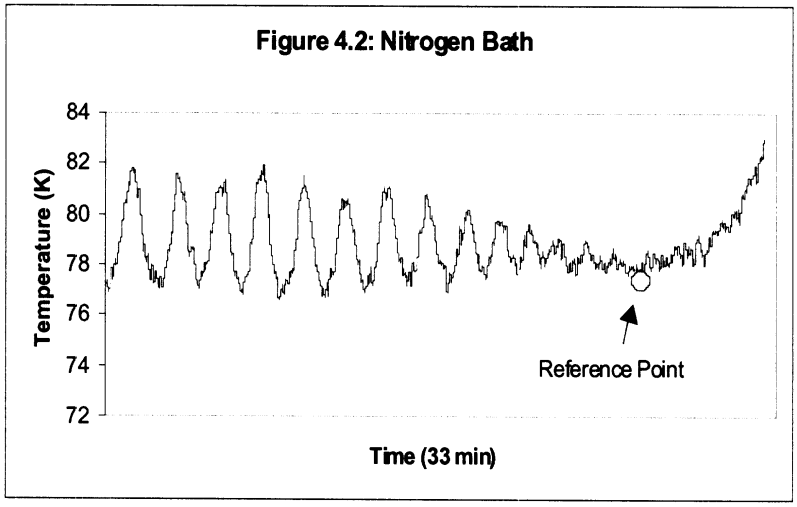

4.1.2 H_2O and Alcohols

Water and alcohol were thought to be good calibration targets due to the availability of dielectric models that computed their complex permittivity. From this we could determine their reflection coefficient versus incidence angle and then in turn their emissivity. The standard Debye equations, as well as permittivity models from Ellison, Richardson and PIOM were investigated. *Figures 4.3* and *4.4* show the real and imaginary part of the permittivity of water at the stated frequencies.

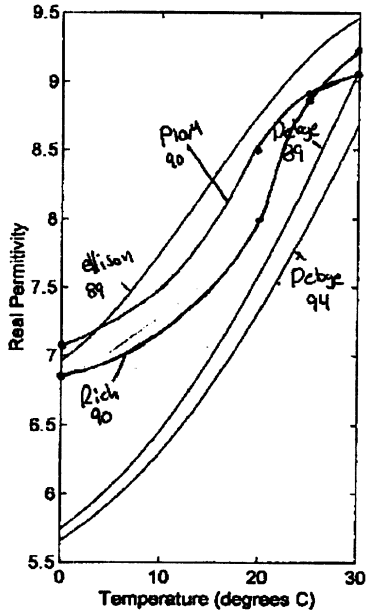

Figure 4.3: Real permittivity

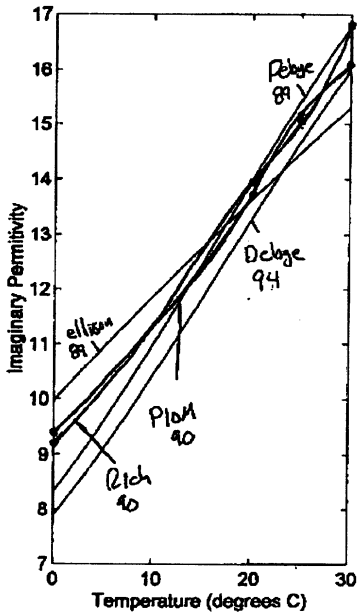

Figure 4.4: Imaginary permittivity

The conclusion is that there is no exact model for water in the millimeterwave region and that the Debye equations become even less reliable at temperatures near 0° C. The Debye equations tend to underestimate both ε' and ε" in the temperature range of 0° to 20° C at frequencies of around 90 GHz. A similar conclusion was drawn for another possible calibration target, ethylene glycol. Inherent in these models at a given frequency is a bias that we are now attempting to determine through accumulation of independent samples. If this bias level can be found, these targets will prove useful.

To use these materials in calibration, we simply measure sky directly and then sky reflected off of a bath of the material. The measured emissivity of the water and alcohol can then be calculated using *Equation 4.3*. T_{Sky} will of coarse be needed and is given by the transfer function of the system obtained by a preliminary hot and cold calibration.

The radiometer was set as shown in *Figure 4.6c* to view sky radiation reflecting off of a bath of water or alcohol at incidence angles of between 14° and 25°. An aluminum plate was then placed on top of the water so that sky alone could be measured at the same angle and then factored out of the water measurement. We then compared the measured and calculated values of emissivity for water and ethylene glycol as shown in the table bellow.

CALIBRATON FLUIDS: EMISSIVITY[15] (θ_{INC} = 14° TO 26°)			
H_20 MEASURED	H_20 CALCULATED	ETHYLENE GLYCOL MEASURED	ETHYLENE GLYCOL[16] CALCULATED
0.738	0.6441	0.935	0.9924
0.749	0.6201		
0.726	0.6103		

Measurements of water had been taken on three occasions. The difference between the measured and calculated data for H_20 suggests a bias level of –0.1128 with a standard deviation of 0.018. Of course, many more measurements must be taken to be confident in this conclusion.

4.1.3 Sky Brightness Temperatures

Models for sky brightness temperatures are also available and were used to verify the use of sky as a valuable calibration target. Sky brightness temperatures were calculated based on pressure, relative humidity, ground level air temperature, and water vapor density, which is in itself a function of temperature and relative humidity. Experiments again showed the possibility of a bias level that we are now trying to determine. The sky brightness temperature model assumes a standard atmosphere and is too general, which could explain the bias.

The measured and calculated sky temperatures are shown in the table below. The reason for the discrepancy between the calculated and measured brightness temperatures is most likely due to the fact that the computer program is based on a standard atmosphere, which is not the case for our measurements. It is believed that a large population of independent samples will lead to a reliable calibration point for sky temperatures.

SKY BRIGHTNESS TEMPERATURES (K)		
ZENITH ANGLE	MEASURED	CALCULATED
Data Set 1 (Air Temp = 7.2° C)		
0°	23.6	43.2
25°	33.8	47.2

4.1.4 Alternative Calibration

A simpler and more reliable method of obtaining the *emissivity transfer function* begins by taking three measurements using the setup configuration in *Figure 4.6C*. First ambient air temperature absorber is placed on top of the target and measured. Then the absorber is removed and the target + sky is measured. Then the target is removed were underneath lies a metal reflector, so sky is measured directly. The following three equations result,

[15] For TM wave.

[16] The model for ethylene glycol is a 2nd order Debye relation.

$$V_1 = [T_0 - T_{ab}]A + b$$
$$V_2 = \left[T_0 - \{T_{phy}e + T_{Sky}(1-e)\}\right]A + b \qquad (4.4)$$
$$V_3 = [T_0 - T_{Sky}]A + b$$

where,
V_1, V_2, and V_3 are the voltage outputs of the radiometer system,
T_0 = the internal temperature of the radiometer (45° C),
T_{ab} = the temperature of the absorber,
T_{Sky} = the sky brightness temperature
T_{Phy} = the temperature of the target, and
e = the emissivity of the target

The multiplicity coefficient A combines a number of system constants including gains, losses, efficiencies, bandwidth, and Boltzmann's constants. Due to Boltzmann's constant, A tends to be very small and has been measured to be between 3 and 10 μ volts per Kelvin. The bias term b is unimportant for this discussion.

By combining the three equations above we have,

$$e = \frac{V_2 - V_3}{V_1 - V_3 + A(T_{ab} - T_{phy})} = a'' + b'' V_2 \qquad (4.5)$$

where b has subtracted out. If $T_{ab} = T_{Phy}$, and V_1 and V_3 remain constant, we have the transfer function that converts the measured V_2 into the targets emissivity. Even if $T_{ab} \neq T_{Phy}$, it is possible to measure A accurately enough for reliable measurements. The main advantage of this calibration system is that it is free from all of the difficulties and limitations of liquid nitrogen saturated absorber. The V_1 measurement is obtained from absorber and as long as its temperature remains close to the physical temperature of the target, it only needs to be taken once. V_3 is obtain from the sky brightness temperature and short-term atmospheric changes could lead to errors in measurement. Changes of up to 7 Kelvin in a short period of time are not uncommon. Consequently, if T_{App} includes T_{Sky}, sky measurements should be taken often and immediately preceding or following sample measurements.

4.2 Sensitivity Measurements

If we assume that the gain of the system does not fluctuate appreciably during the measurement period, the theoretical sensitivity of a Dicke radiometer is given by:

$$\Delta T = 2 \cdot \frac{T_{App} + T_N}{\sqrt{B\tau}} \qquad (4.6)$$

where, T_N is the system noise temperature of the radiometer, B is the bandwidth, and τ is the integration time. The system noise temperature can be calculated by adding the noise figures and losses of the front end of the radiometer to obtain a total noise figure (NF) and then converting this to an equivalent noise temperature as follows.

mixer-preamplifier	6.5 dB
isolator	1.2 dB
ferrite circulator	1.2 dB
waveguide	0.2 dB
Total:	**9.1 dB**

This is equivalent to a noise temperature of (9.1 dB ~ 8.3),

$$T_N = 290(NF - 1) \approx 2100\ K \qquad (4.7)$$

Then from *Equation 4.6* above the sensitivity of 94 GHz radiometer with a one second integration time viewing a room temperature (20° C) target is at best 0.2 K. Sensitivity measurements were taken using room temperature absorber and liquid nitrogen saturated absorber as hot and cold calibration loads respectively. With a 1-second integration time constant, sensitivity measurements performed to date have varied from minimums of approximately 0.2 to maximums of approximately 0.7. The data indicate an average sensitivity of 0.34 K, which suggests a system noise temperature of approximately 5,300 K and a front-end noise figure of 12.8 dB. Some of the added noise can be attributed to the Dicke switch. It is possible to tune the current driver to optimize the insertion loss of the circulator but this was not done.

Sensitivity measurements were taken at different time constants as shown in the table below. Using $\tau = 1$ sec. as a reference, the theoretical sensitivities for the other time constants were calculated using *Equation 4.6* and are also shown. Theory predicts that the sensitivity of a Dicke Radiometer will be proportional to one over the square root of the time constant. The measured data shows clearly that the sensitivity does not vary in this way. Some investigation as to why this is the case has been done and it is believed that the answer lies in the way the lock-in amplifier processes the input data, but a full explanation is pending.[17]

TIME CONSTANT (S)	SENSITIVITY (K) MEASURED	SENSITIVITY (K) THEORY
0.03	1.2	1.9
0.1	0.73	1.0
0.3	0.62	0.58
1	0.32	0.32

The sensitivity of the system was measured using different Dicke switch frequencies as shown in the table below. To enhance stability due to gain fluctuations we decided to use the higher frequency of 750 MHz. This is well within the allowed range of 100 to 1000 Hz.

FREQUENCY (HZ)	SENSITIVITY (K)
390	0.20
505	0.31
750	0.26

4.3 Stability Measurements

A series of experiments were performed to determine the stability to the radiometer and establish the required frequency of calibration. The system was calibrated using a hot and cold load, as mentioned previously, at periodic times throughout a five-hour period. Allowing an hour for warm up, the mean sensitivity in the preceding four hour period was 0.22 K, with a standard deviation of 0.03 K. The calibration at the one-hour mark was then used as a reference to examine the stability of the system. The mean hot load temperature, as determined by the radiometer, was 294.8 K, a difference of 0.1 K from the physically measured temperature. The hot load standard deviation was 0.7 K. The mean cold load temperature, as determined by the radiometer, was 77.05 K, a difference of 0.35 K from 77.4 K[18], the boiling temperature of N2. The cold load

[17] For instance, the filter roll-off value effects sensitivity independent of τ. Also, the manual for the lock-in recommends a waiting period of 4 seconds before reading data when τ is set at 1 second. The actual relationship between τ in equation (5) and the time constant setting on the lock-in is, at best, vague.

[18] To measure drift, we chose the boiling point of N2 as the reference. Its actual temperature is not known or needed here.

standard deviation was 0.6 K. For our application temperature stability of < 1 K is insignificant and calibration does not need to be repeated in a four hour period.

Most of the measurements performed in the beginning of the project were conducted in the laboratory, but when the system was taken on the roof of the EECS building to take sky brightness measurements, the output voltage was noticeably effected by the location of persons positioned near the radiometer. Stability and sensitivity suffered, ballooning to between 2 and 5 Kelvin over short time intervals. Also during measurements, it was noticed that variations in voltage output occurred when the cables connecting the radiometer to the lock-in and/or power supplies were moved, touched, or jostled. Ground loops where suspected and after many tests involving the use of different cables, better shielding and better isolation of power and signal lines, the interference effects were reduced, but not eliminated. To improve system performance, the Dicke switch driver was moved from the power supply box to the radiometers insulated case. Finally the stability of measurements were improved by simply staying away from the radiometer system while measurements were in progress.

The radiometer was run for a period of 40 hours to investigate the possibility of drift occurring in the output voltage. The radiometer was in a semi-secluded area of the laboratory viewing a room temperature absorber. Aside from a few small anomalies, the RMS variation in the output did not exceed 3-uV which, equates to a change in apparent temperature of less than 0.6 Kelvin (*Figure 4.5*). Normal temperature fluctuations in the room were not factored into this result which indicates that this is probably an over estimate of the actual system drift.

Figure 4.5: Stability Measurements

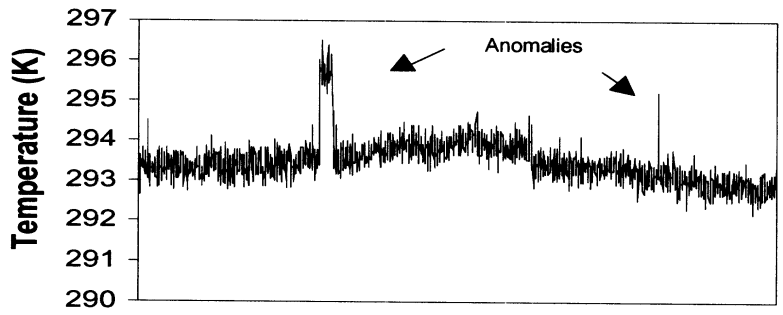

4.4 Measurement Configurations

Figure 4.6 displays all of the measurement configurations used in our experiments. *Figure 4.6A* is a standard target measurement. The radiometer is viewing the target's emission plus the sky reflected off of the target surface. The process is characterized in *Equation 4.2* where $T_{inc} = T_{Sky}$, and T_{Phy} and e are the temperature and emissivity of the target respectively. By taking the target off of the copper plate, the sky brightness temperature may be measured directly and used to calculate the emissivity of the target using *Equation 4.3*. The angle of the copper plate with respect to the ground is generally close to 45°[19] but the exact angle is unimportant as long as it remains constant for both measurements.

[19] Sky is viewed at zenith.

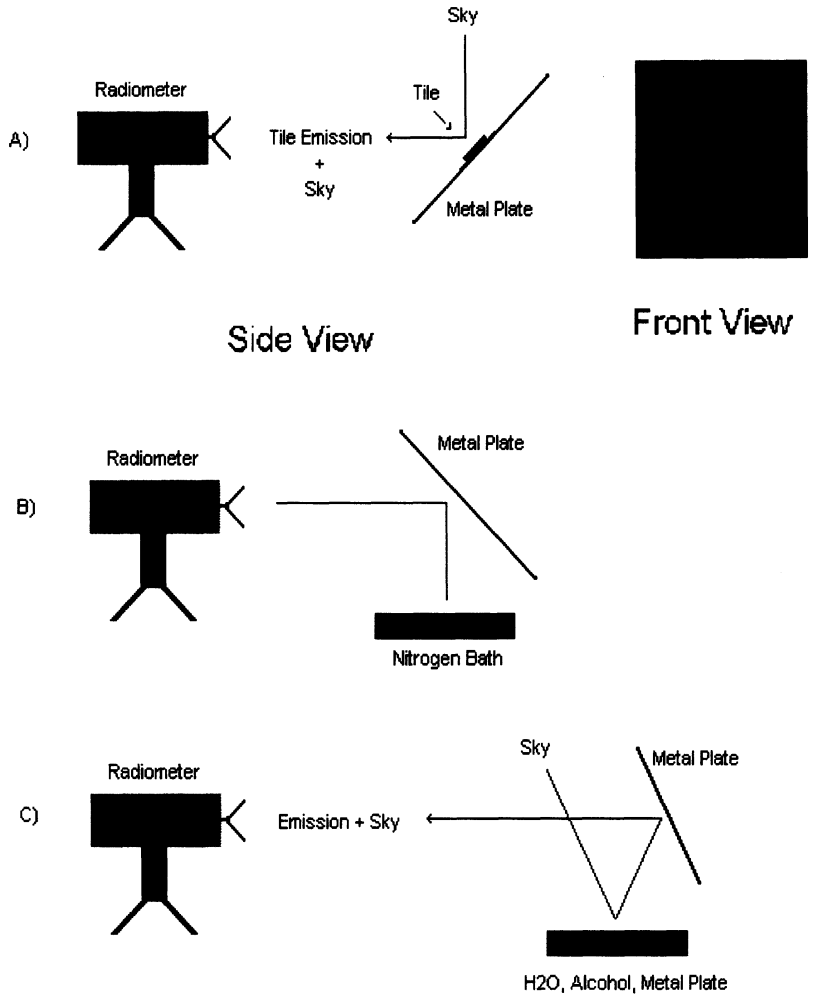

Figure 4.6: Measurement configurations

Figure 4.6B shows our method of obtaining a cold load calibration measurement. Here we used a metal plate to reflect the beam of the antenna onto the N2 saturated absorber at near vertical incidence. The angle that the plate makes with the ground is approximately 45°. Absorber at ambient air temperature is also measured in this way. The apparent temperature of the scene is equal to the physical temperature of the absorber, since $e = 1$ for the absorber.

Figure 4.6C shows a very versatile measurement configuration where the sky radiation is reflected off of the target and again off of the copper plate into the radiometer. The target emission is also reflected from the copper plate and thus combined with the sky upon entry into the radiometer. The result is identical to setup *A* except that; 1) Zenith angles near zero are restricted by the blockage of the metal plate, and 2) targets may be placed level to the ground which is a necessity when measuring liquids. All targets can be measured using configuration *C*.

In some measurement configurations absorber is measured at incidence angles other than 0°. Experiments were performed to investigate the reliability of off axis measurements of absorber. Absorber was measured at angles ranging from normal to 50° and the results are shown in *Figure 4.7* below. For our application the temperature variations at angles below 30° are insignificant.

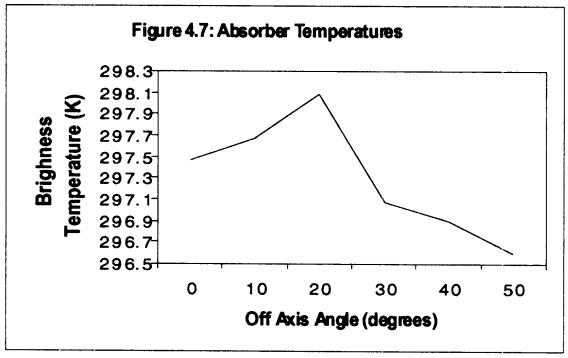

We may at times be measuring planar targets with finite reflection coefficients at normal incidence. Experiments were conducted in order to determine if and how much energy is emitted from the radiometer through the antenna. Any emission from the radiometer would be reflected back into itself causing erroneous readings. The experiment was performed by placing a copper plate normal to the antenna and in the far field. Initial results showed that either a very high or very low apparent temperature was being emitted. A phase reversal in the output square-wave of the radiometer confirmed that extremely high brightness temperatures were being emitted (>700 Kelvin). Measurements at normal incidence must therefore be avoided. There is an isolator between the balance mixer and the rest of the front end and one would expect to see a temperature that is at most, equal to the internal temperature of the radiometer (45° C ~ 319 K). We suspect that the LO has sufficient power to bypass the 20 dB isolator and thus could be responsible for this result. To produce a temperature of 700 K at the radiometer, a power level of,

$$P = kT_{App}B = -83\ dBm \tag{4.8}$$

would have to leak past the isolator, which, is not unbelievable.

4.5 Tile Measurements

Although the absolute calibration of the radiometer had not yet been done to our satisfaction, the system was stable and had adequate sensitivity with a one-second integration time. Initial tile measurements were therefore performed to examine the validity of the direction of the project. NASA/Ames provided two tile samples, one of which was in new condition and the other simulated TPS failure with a charred SIP layer, thus leaving a gap of air between the aluminum plate and the RSI. *Figure 4.8* shows the damaged tile on the left and the undamaged tile on the right.

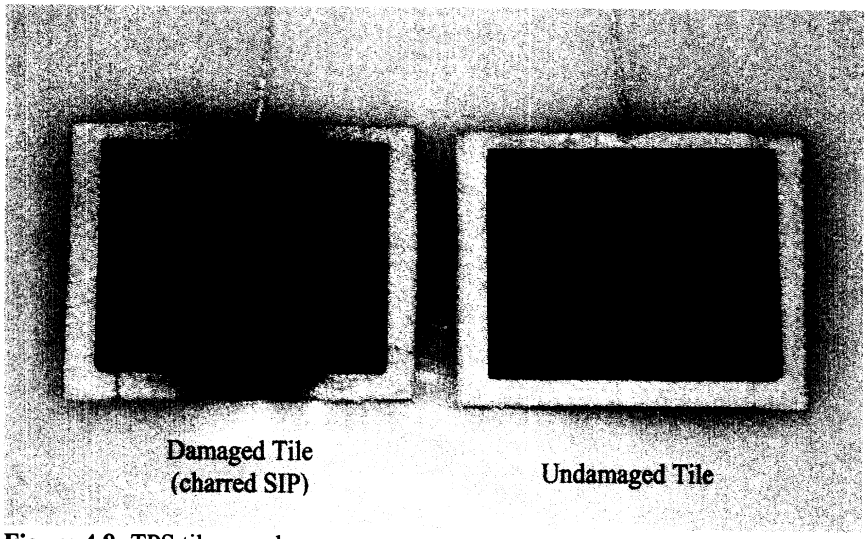

Figure 4.8: TPS tile samples.

The setup for this experiment is shown in *Figure 4.6A* with a tile placed on the reflecting surface so that the radiometer is reading a combination of emissivity from the tile, and sky reflecting from the tile's specular surface. The tile samples were measured with vertical polarization using the standard setup at a close range of 2 meters to ensure a beam-filling (6-dB) tile and to alleviate the need for exact positioning of the tiles. The results of this experiment show that there is approximately a 10 Kelvin change in apparent temperature between the damaged and undamaged tiles. The sensitivity of the system is consistently below 1 K so we can conclude that this type of TPS failure is highly detectable. Using *Equation 4.3*, and with the sky removed, the emissivity of the tiles is shown to vary by approximately 0.033. *Figure 4.9* shows the emissivity[20] of the two tiles over time. The radiometer first viewed the undamaged tile and then the damaged tile repeatedly.

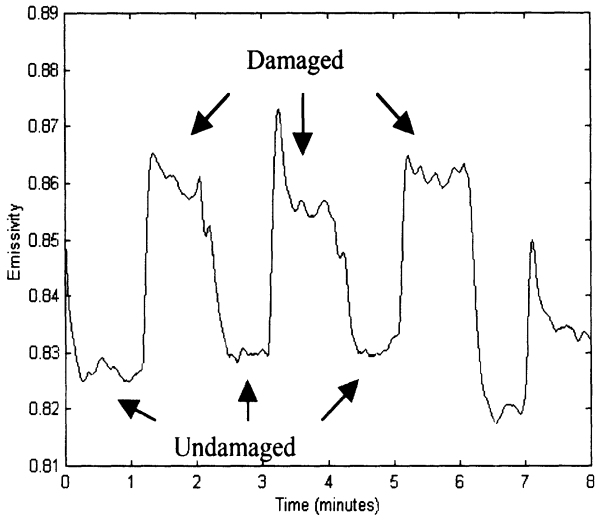

Figure 4.9: Tile emissivity.

Also, from our simulations horizontal polarization is expected to be as much as twice as sensitive to this type of failure. The sensitivity of the 94 GHz radiometer to emissivity changes is given by,

$$\Delta e = \frac{V_{rms}}{V_3 - V_1} \approx 0.0014 \tag{4.9}$$

Compared to the model in *Section 2.3* the measured tiles have an obvious increase in loss. This is evident from the damaged tile's increase in emissivity. In *Figure 2.9* the total change in emissivity from an air gap of zero to an air gap of 4 mm is –0.042. Conversely the measured difference is +0.033. Possible errors in the model may include:

(1) The RTV glue was not modeled and may contribute to additional loss.
(2) Incorrect permittivity values for the RSI and SIP.
(3) The measured tile samples where beam filling to only a 6-dB beam-width. Therefore, edge effects could be present that were not modeled in the simulation.
(4) Near-field effects were not modeled.

The measurement of a new larger sample (24" x 24") provided by NASA/Ames will resolve the possible errors of (3) and (4). We will deal with (1) and (2) by measuring the dielectric constants of the RTV, RSI, and SIP with the 94 GHz radiometer system.

[20] The apparent temperature is a combination of the tile emissivity and the sky brightness temperature.

4.5.1 Tile Size Considerations

The tile samples were approximately 6" x 6" and, as mentioned previously, we needed to place the tile in the far field of the antenna to obtain consistent measurements. To maximize the output response to tile discrepancies and to minimize the care needed in tile positioning, the tiles must also be beam filling at the 6-dB beamwidth of the antenna. If the tiles were not beam filling, when comparing one square tile to the next, they would have to be positioned with the exact same orientation. We would then know that any changes in output resulted from actual emissivity differences in the tiles and not from changes in stray radiation beyond the edges of the tile from sky or other sources. To demonstrate this we conducted an experiment (refer to *Figure 4.10*). Using the standard setup (*Figure 4.6A*) a tile was placed in the center of the antenna beam at a distance of two meters. Its apparent temperature was then measured at zero lateral displacement, at 1 cm displacement, at 2 cm, and then at 3 cm. For a 1 cm displacement the apparent temperature dropped approximately 4 K and for 2 cm the temperature dropped about 20 K. Thus increased sky emission is seen by the radiometer due to the displacement of the tile. Increasing the size of the target will eliminate this effect and yield more reliable measurements.

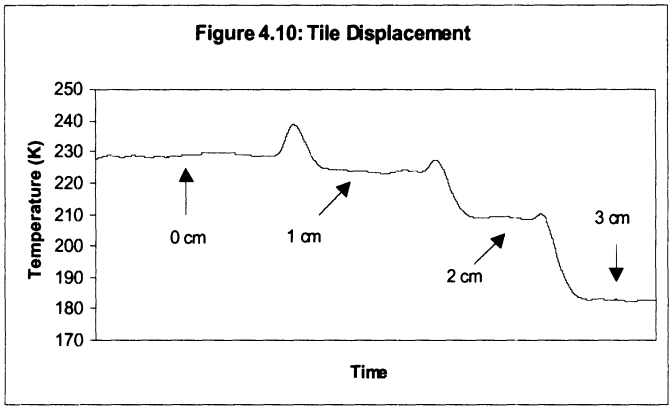

Next we measured a single TPS tile at varying distances from the antenna to see how far away it could be and still be beam-filling. The 6-dB spot size of the antenna was calculated to be approximately 2 in/m, which suggests a 3-meter maximum distance for tile measurements. This is below the 5-meter minimum we have suggested previously due to antenna concerns. *Figure 4.11* charts the response of the radiometer to the 6-inch tile at varying distances.

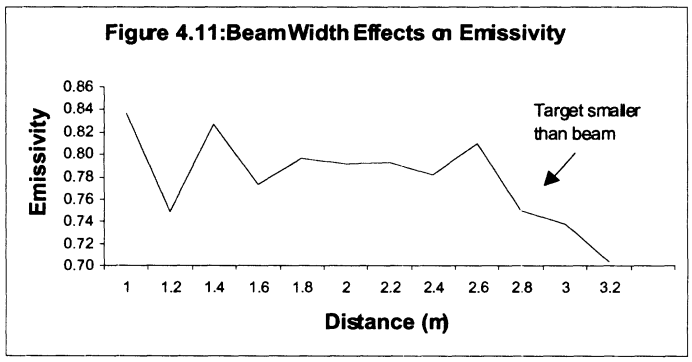

Experiments showed that our samples were too small and that beyond 2.5 meters the apparent temperature of the tile changed dramatically, indicating that the main beam of the antenna was outside the edges of the tile and receiving pure sky emission. New, larger tile samples have since been provided by NASA.

In order to obtain more evidence of the effects of near field measurements on the radiometer system we conducted and experiment to view sky brightness temperatures using the standard setup

at varying distances from the antenna. It is suspected that placing the copper plate close to the antenna produces a pattern deformation and possibly mismatches at the antenna receiver terminals. *Figure 4.12* shows our results. As you can see, the effect of the metal ground plane is significant and consistent measurements can only be obtained beyond 3 meters.

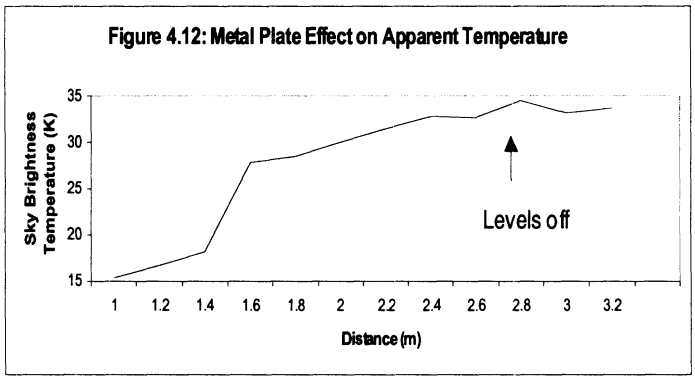

5.0 Conclusions

The permittivity of TPS materials indicates that millimeterwave detection of TPS failure will be possible. TPS materials are transparent and simulations show that changes in emissivity and brightness temperature are within the detectable range of radiometer systems. We have designed a 94-GHz radiometer system with a sensitivity of 0.34 K.

Experiments with the radiometer system show that TPS failure due to charred SIP is readily detectable through variations in tile emissivity. One can distinguish between the clutter or background radiation and the small changes in signal caused by changes in TPS material properties by masking background radiation with cold brightness temperature emission. The 94-GHz radiometer detected the 0.033 difference in emissivity caused by charred SIP and was sensitive to changes in emissivity of 0.0014. Our system was designed for laboratory measurements using available parts and much higher sensitivities are achievable on modern radiometer designs.

Changes in emissivity and changes in local temperature may be distinguished by measuring the targets physical temperature thus eliminating it as a variable. This is done in one of two ways. The first uses the experimental setup shown in *Figure 4.6A* and *Equation 4.3*. The second uses the experimental configuration shown in *Figure 4.6C* and measures absorber, sky and then the target-sky combination. By applying *Equation 4.5* the emissivity of the target is again obtained.

Sufficient transverse spatial resolution can be achieved to localize the damaged area by use of millimeter wavelengths and large aperture antennas. The large apertures may be achieved by using real beam sharpening techniques such as lenses or by 'synthetic' electrical means. These systems are limited to resolutions of a fraction of a wavelength. We can accelerate the measurement process and hence reduce the time for inspection by using short integration times, scanning the antenna beam either electrically or mechanically, and by automating the process.

To distinguish between different types of damage further work must be done. Two techniques may be used: (1) Simulations can be performed based on information from NASA/Ames detailing the types of failures that may be present. (2) Experiments can be done to characterize the response of the 94 GHz radiometer system to the various failure modes.

5.1 Project Plan

There are a number of issues yet to be resolved prior to implementation. The remainder of the project will lead to their resolution.

- Which calibration method is simplest and most reliable. Either technique described in *Section 4.1* may be used depending on how the system is deployed.
- How to achieve adequate resolution? A synthetic aperture technique may be used or possibly beam focussing. Cost and system complexity will be considered.
- What is the best choice of technique to resolve ambiguities due to emissivity oscillations as described in *Section 2.3*. The choices include using a two-frequency or two-angle technique and will include a cost vs. complexity trade-off.
- Minimum sensitivity requirements of the final system must be set. A cost vs. speed of measurement trade-off will ensue concerning how to best achieve the desired sensitivity. State-of-the-art radiometers will achieve the best sensitivities allowing a decrease in the integration time, thus speeding up the measurement.
- Whether to use mechanical or electrical scanning or a combination of both?

As a follow-up to this study, we recommend the following activities:

- Characterize the permittivity of the TPS materials including the Reusable Surface Insulation (RSI), the Strained Isolation Pad (SIP), and bonding materials.
- Use these results to further simulate TPS emission.
- Measure various larger tiles, both damaged and undamaged, to se how well the proposed technique works.
- Measure other dielectric materials used in "new age" TPS designs.
- Model "enhanced" bonding materials or tile coatings designed to change permittivity in response to excessive thermal stress.
- Design implementation of an automated radiometer system for TPS remote failure detection.
- Investigate existing technology, design, and build prototype.
- Test prototype.
- Implement prototype at NASA facilities.
- Re-evaluate project direction (modify of redesign).
- Finalize documentation.

Appendix A: 94 GHz Radiometer Component Specifications

94 GHz lens-corrected horn
Alpha W858-6 High Efficiency Horn Lens Antenna

SPECIFICATIOINS	
Frequency	94 GHz
Diameter	6"
3 dB Beam Width	1.45° E, 1.45° H
6 dB Beam Width	3° E, 3° H
Main beam Width	4.8° E, 5.7° H
1st Side Lobe Level	28.2 dB E, 29.3 dB H
Polarization	Vertical
Efficiency	> 55%
Main Beam Efficiency	90% ± 5%

W-band ferrite switch
Alpha W140 Medium Power Reciprocal Switch

SPECIFICATIONS	
Frequency	94 GHz
Insertion Loss (main)	1.93 dB
Insertion Loss (ref)	1.89 dB
Isolation (main)	30.2 dB
Isolation (ref)	27.8 dB
VSWR Max.	1.35
Peak Power	0.5 kW
Average Power	1.5 W
Bandwidth	2%
Coil Resistance	5 ohms
Coil Inductance	2 mH
Switching Speed	2-5 usec
Current Drive	0 – 250 mA

94 GHz isolator
Millitech (115)

SPECIFICATIONS	
Frequency	94 GHz
Bandwidth	2%
Isolation	19.5 dB
Insertion Loss	0.75 dB

94.2 GHz Local Oscillator
Millitech GDV-10-05160 varactor-tuned Gunn diode oscillator

SPECIFICATIONS (41.5° C)	
Center Frequency	94.5 GHz
Power Output	40 mW min.
Tuning Range	± 250 MHz
Operating Voltage	10.2 Vdc
Varactor Voltage Range	0 to +16 Vdc

Varactor Voltage is set at 1.5 Vdc to maintain a 94.2 GHz output frequency.

Mixer
Hughes 47476H-1211 W-band waveguide balanced mixer w/IF amplifier

SPECIFICATIONS (25° C)	
Frequency	94 GHz
Noise Figure	5 dB
Bandwidth	4%
RF Input VSWR max.	2:1
LO Drive Power	+5 dBm
RF-LO Isolation	20 dBm
LO Noise Suppression	35 dB
RF-IF Gain min.	20 dB
Input Voltage	+15 Vdc
DC Current	30 – 50 mA
IF Band	10 – 510 MHz

Amplifier
Miteq AM-3A-000110 Amplifier

SPECIFICATIONS	
Frequency Range	1 – 1000 MHz
Gain	36.9 ± 0.35 dB
Noise Figure (max.)	1.65 dB
Input Voltage	+15 Vdc
DC Current	65 mA

Crystal Detector
Hewlett Packard 8473B

SPECIFICATIONS (25° C)	
Frequency Range	0.01 – 18 GHz
Frequency Response	± 0.2 dB over any octave to 8 GHz
Max. Input Power	200 mW
Low Level Sensitivity (< -20 dBm)	0.4 mV/uW (40° to 55° C)
SWR	1.2 up to 4 GHz
Input Impedance	50 Ohm
Output Impedance	1 to 2 K with 20 to 60 pF

Regulator board and resistive network

Both amplifiers are regulated with the National Semiconductors LM2940CT-15.

SPECIFICATIONS (25° C)	
Output Voltage	15 Vdc
Line Regulation	150 mV max

Load Regulation	150 mV max
Output Noise Voltage	450 uV max
Ripple Rejection	52 dB min
Long Term Stability	60 mV/1000 Hr
Dropout Voltage	150 mV max
Maximum Line Transient	45 Vmin

The varactor tuning voltage is regulated with the National Semiconductors LM2940CT-5. The 5-volt output is then past through a resistive network that outputs the 1.2 Vdc frequency control voltage.

SPECIFICATIONS (25° C)	
Output Voltage	5 Vdc
Line Regulation	50 mV max
Load Regulation	50 mV max
Output Noise Voltage	150 uV max
Ripple Rejection	60 dB min
Long Term Stability	20 mV/1000 Hr
Dropout Voltage	150 mV max
Maximum Line Transient	45 Vmin

The LO input Voltage is regulated with the National Semiconductors LM2940T-10.

SPECIFICATIONS (25° C)	
Output Voltage	10 Vdc
Line Regulation	100 mV max
Load Regulation	100 mV max
Output Noise Voltage	300 uV max
Ripple Rejection	51 dB min
Long Term Stability	36 mV/1000 Hr
Dropout Voltage	150 mV max
Maximum Line Transient	60 Vmin

Dicke Switch current driver*

Resistive heating element
Omegalux SRFR-36/5 flexible silicon rubber heater.

SPECIFICATIONS	
Dimensions	3x6 in.
Power Density	5 W/in^2
Total Power	90 W
Input Voltage	115 volts ac

Lock-In Amplifier
Stanford Research SR850 DSP Lock-In Amplifier

SPECIFICATIONS	
Signal Channel	
Sensitivity	2 nV to 1V
Impedance	1 MΩ + 25 pf
Gain Accuracy	1 %
Noise	6 nV @ 1 kHz
Dynamic reserve	0 to 100 dB
Internal Oscillator	
Frequency Range	0.001Hz to 102 kHz
Distortion	-80 dBc
Amplitude	0.004 to 5 Vrms
Output Impedance	50 Ω
Outputs	Sine and TTL
Demodulator	
Stability	No drift
Harmonic Rejection	-90 dB
Time Constants	10 us to 30 ks (6, 12, 18, 24 dB/oct rolloff)
Display	
Display Types	Numeric w/bar graph, polar or strip chart
Data Buffer	64k data points can be stored and displayed as strip charts.
Sample Rate	512 Hz to 62.5 MHz
Analysis Functions	
Smoothing	5, 9, 17, 21, or 25 point
Curve Fitting	Linear, exponential, or Gaussian
Calculator	Arithmetic, Trigonometric, and logarithmic on trace region.
Statistics	Mean and standard deviation of trace region.
General	
Disk Drive	3.5 in. MS-DOS compatible format 720 kbyte capacity.
Power	60 W, 115 Vac
Dimensions	17"W x 6.25"H x 19.5"L
Weight	40 lbs.